

See discussions, stats, and author profiles for this publication at: <https://www.researchgate.net/publication/321949024>

Synthesis of $\text{Cu}_2(\text{Zn}_{1-x}\text{Co}_x)\text{SnS}_4$ nanocrystals and formation of polycrystalline thin films from their aqueous...

Article in *Journal of Materials Chemistry A* · January 2018

DOI: 10.1039/C7TA06295H

CITATIONS

0

READS

62

5 authors, including:



Alexandre Henrique Pinto

Ithaca College

7 PUBLICATIONS 33 CITATIONS

SEE PROFILE



Seung Wook Shin

University of Toledo

108 PUBLICATIONS 1,968 CITATIONS

SEE PROFILE



Eray Aydil

University of Minnesota Twin Cities

229 PUBLICATIONS 10,571 CITATIONS

SEE PROFILE

Some of the authors of this publication are also working on these related projects:



Current project. [View project](#)



Low-k dielectric materials [View project](#)



Cite this: DOI: 10.1039/c7ta06295h

Synthesis of $\text{Cu}_2(\text{Zn}_{1-x}\text{Co}_x)\text{SnS}_4$ nanocrystals and formation of polycrystalline thin films from their aqueous dispersions†

Alexandre H. Pinto, ^{‡§a} Seung Wook Shin, ^{‡¶b} Aastha Sharma, ^c
R. Lee Penn ^{*a} and Eray S. Aydil ^{*b}

Quintenary $\text{Cu}_2(\text{Zn}_{1-x}\text{Co}_x)\text{SnS}_4$ is an analog of the promising solar absorber material $\text{Cu}_2\text{ZnSnS}_4$ (CZTS). The initial rapid progress in CZTS has stalled because the similar sizes of Cu and Zn cations lead to facile formation of antisite defects, which are thought to limit the solar cell performance. Cobalt substitution for Zn may reduce cation disorder. Herein, we report the synthesis of wurtzite $\text{Cu}_2(\text{Zn}_{1-x}\text{Co}_x)\text{SnS}_4$ across the entire composition range and a systematic study of the substitution of Co into the wurtzite CZTS lattice. The synthesis is based on microwave heating to only 160 °C and uses metal salts and thiourea as precursors and ethylene glycol as the solvent. The $\text{Cu}_2(\text{Zn}_{1-x}\text{Co}_x)\text{SnS}_4$ nanocrystals were phase pure wurtzite within the detection limits of X-ray diffraction and Raman scattering. The wurtzite lattice parameters, nanocrystal sizes, and A1 Raman mode peak positions depend on the Co concentration, x . The lattice parameters follow Vegard's law within the accuracy of our measurements, and the A1 Raman mode shifts nearly linearly with x . The nanocrystal size decreases from 8 nm to 4 nm as x increases from 0 to 1. The absorption band edge blue shifted from 1.1 eV for $x = 0$ to 1.35 eV for $x = 1$. These values are lower than those predicted by density functional theory calculations and previous attempts at determining the optical band gap for wurtzite $\text{Cu}_2\text{ZnSnS}_4$ ($x = 0$) and $\text{Cu}_2\text{CoSnS}_4$ ($x = 1$). Either the band gaps of wurtzite $\text{Cu}_2\text{ZnSnS}_4$ ($x = 0$) and $\text{Cu}_2\text{CoSnS}_4$ ($x = 1$) are lower or these materials have significant band tails due to defects. We also prepared polycrystalline $\text{Cu}_2(\text{Zn}_{1-x}\text{Co}_x)\text{SnS}_4$ thin films by thermal annealing, in sulfur, of coatings comprised of $\text{Cu}_2(\text{Zn}_{1-x}\text{Co}_x)\text{SnS}_4$ nanocrystals. Upon annealing in sulfur, the wurtzite $\text{Cu}_2(\text{Zn}_{1-x}\text{Co}_x)\text{SnS}_4$ nanocrystals transformed into larger grains (100 s of nm to microns) that have a kesterite structure. The films with $x \leq 0.4$ were phase pure kesterite within the detection limits of XRD and Raman scattering, but, for $x \geq 0.6$, secondary phases such as $\text{Cu}_{1.96}\text{S}$ and $\text{Co}_{0.24}\text{Zn}_{0.76}\text{S}$ were also detected.

Received 18th July 2017
Accepted 20th November 2017

DOI: 10.1039/c7ta06295h

rsc.li/materials-a

Introduction

Kesterite $\text{Cu}_2\text{ZnSnS}_4$ (CZTS) and the related compound $\text{Cu}_2\text{-ZnSn}(\text{S}_x\text{Se}_{1-x})_4$ (CZTSSe) are being considered as absorber

layers in thin-film solar cells^{1,2} because they have high absorption coefficients in the visible range of the electromagnetic spectrum³ ($>10^{-4} \text{ cm}^{-1}$), direct and easily tunable band gaps between 1.0 eV and 1.5 eV by adjusting the S-to-Se ratio,⁴ and a high theoretical efficiency ($\sim 32\%$).⁵ Moreover, CZTSSe is comprised of abundant metals with low toxicity relative to other solar cell materials such as CdTe. Although CZTSSe-based thin-film solar cells have already achieved a record efficiency of 12.7%,⁶ this performance still falls significantly short of the 21.7% efficiency of $\text{Cu}(\text{In,Ga})\text{Se}_2$ (CIGS)-based solar cells⁷ and of theoretical efficiencies (32.4% for CZTS and 31% for CZTSSe).⁸

Alarming, the initial rapid rise achieved in record efficiencies between 2010 and 2014 has stalled. Among the reasons responsible for this underperformance is the relatively large open circuit voltage, V_{oc} , deficit (600 mV) with respect to the theoretical maximum (*i.e.*, the band gap, E_g , divided by the electron charge).^{9,10} This deficit is much larger for CZTSSe than for CIGS-based solar cells (440 mV).⁶ One possible reason proposed for this relatively high V_{oc} -deficit is band gap and

^aDepartment of Chemistry, University of Minnesota, 207 Pleasant Street SE, Minneapolis, MN 55455, USA. E-mail: rleppenn@umn.edu

^bDepartment of Chemical Engineering and Materials Science, University of Minnesota, 421 Washington Ave. SE, Minneapolis, MN 55455-0132, USA. E-mail: pinto039@umn.edu

^cDepartment of Chemistry, University of Illinois at Urbana-Champaign, 600 South Mathews Avenue, Urbana, IL, 61801, USA

† Electronic supplementary information (ESI) available. See DOI: 10.1039/c7ta06295h

‡ Equal first authors.

§ Present address: Department of Chemistry, Ithaca College, Center for Natural Sciences, 953 Danby Road, Ithaca, NY 14850, USA.

¶ Present address: Department of Physics and Astronomy and Wright Center for Photovoltaic Innovation and Commercialization, University of Toledo, Toledo, OH, 43606, USA.

band edge fluctuations due to cation disorder and antisite defects such as CuZn, ZnCu, ZnSn, and SnZn.^{11,12} Moreover, Cu and Sn have multiple oxidation states and favor the formation of deep-level defects in CZTSSe.¹³ These defects may increase the non-radiative carrier recombination rate and lower the V_{oc} .¹¹ Higher V_{oc} values are achieved by substituting some of the cations in CZTSSe. For example, replacing Sn with Ge improves V_{oc} by reducing defect concentrations.¹⁴ The main problem, however, is the similar sizes of Cu^+ (0.91 Å), Cu^{2+} (0.87 Å), and Zn^{2+} (0.88 Å) cations, which allow them to easily substitute for each other resulting in substantial cation disorder in wurtzite and kesterite phases of CZTS.^{10,11} One solution to this problem is to substitute a smaller cation such as Co^{2+} (0.68 Å) for Zn^{2+} (0.88 Å) to form $Cu_2(Zn_{1-x}Co_x)SnS_4$ alloys with band gaps similar to that of CZTS.^{15,16} The smaller size of Co^{2+} is expected to result in reduced cation disorder and antisite defects in Cu_2CoSnS_4 as compared to Cu_2ZnSnS_4 . Thus, $Cu_2(Zn_{1-x}Co_x)SnS_4$ alloys may lead to solar cells with a higher V_{oc} .

In one approach to making polycrystalline thin films for solar cells, CZTS coatings are cast on substrates from nanocrystal dispersions, and the resulting coatings are annealed in sulfur or selenium vapor.^{17–20} CZTS nanocrystals have been synthesized using a variety of routes, and methods for controlling their size and composition have been explored.^{21–24} Making $Cu_2(Zn_{1-x}Co_x)SnS_4$ films using this method will require the synthesis of nanocrystals with the desired cation composition, x . A few studies have reported the synthesis of Cu_2CoSnS_4 nanocrystals.^{25–30} To our knowledge, there is only one recent report of stannite $Cu_2(Zn_{1-x}Co_x)SnS_4$ ($0 \leq x \leq 1$) nanocrystals across the entire composition range: Huang *et al.* synthesized stannite $Cu_2(Zn_{1-x}Co_x)SnS_4$ nanocrystals by reacting metal salts with thiourea in oleylamine for more than 24 hours at temperatures greater than 260 °C.³¹ More recently, Thompson *et al.* synthesized wurtzite $Cu_2(Zn_{1-x}Co_x)SnS_4$ nanocrystals from metal salts in octadecene using trioctylphosphine oxide but only for x between 0 and 0.11. To our knowledge, wurtzite $Cu_2(Zn_{1-x}Co_x)SnS_4$ nanocrystals and polycrystalline thin films have not been synthesized previously across the entire composition range (*i.e.*, $0 \leq x \leq 1$). Moreover, previous synthesis of Cu_2CoSnS_4 nanocrystals used chemicals such as trioctylphosphine oxide and oleylamine,^{25,30,31} which are known to be cytotoxic.^{32,33}

Herein, we report the synthesis of $Cu_2(Zn_{1-x}Co_x)SnS_4$ nanocrystals ($0 \leq x \leq 1$) and thin polycrystalline films formed by annealing coatings cast from dispersions of these nanocrystals. Specifically, we made $Cu_2(Zn_{1-x}Co_x)SnS_4$ nanocrystals using a microwave-assisted solvothermal synthesis in ethylene glycol and investigated the formation of polycrystalline $Cu_2(Zn_{1-x}Co_x)SnS_4$ films on Mo-coated soda lime glass substrates when coatings cast from aqueous dispersions of these nanocrystals are annealed in sulfur vapor. Advantages of microwave synthesis have been reviewed by Baghbanzadeh *et al.*: they include significant reduction in synthesis times and efficient use of energy by coupling it selectively with the solvent.³⁴

Experimental procedure

Materials

Copper(II) acetate monohydrate ($Cu(II)Ac_2 \cdot H_2O$ ACS reagent, >98%, Sigma-Aldrich), zinc acetate dihydrate ($ZnAc_2 \cdot 2H_2O$ ACS reagent Acros Organic), cobalt(II) acetate tetrahydrate ($Co(II)Ac_2 \cdot 4H_2O$, >97%, Acros Organic), tin(II) chloride ($Sn(II)Cl_2$ 98% Sigma Aldrich), thiourea (CH_4N_2S , $\geq 99.0\%$, Sigma Aldrich), sodium thioglycolate ($HSCH_2COONa \geq 96.5\%$, Sigma Aldrich), ethylene glycol (Fisher Scientific), methanol (Sigma Aldrich), and ethanol (Decon-200 Proof) were used as received.

Synthesis of $Cu_2(Zn_{1-x}Co_x)SnS_4$ nanocrystals

In a typical Cu_2ZnSnS_4 synthesis, 1.7×10^{-3} mol of $Cu(II)Ac_2 \cdot H_2O$, 1.0×10^{-3} mol of $ZnAc_2 \cdot 2H_2O$, and 1.0×10^{-3} mol of $Sn(II)Cl_2$ were added to 30 mL ethylene glycol while stirring. To synthesize Cu_2CoSnS_4 , 1.0×10^{-3} mol of $ZnAc_2 \cdot 2H_2O$ was replaced by 1.0×10^{-3} mol of $CoAc_2 \cdot 4H_2O$. To synthesize $Cu_2(Zn_{1-x}Co_x)SnS_4$ solid solutions, the amounts of $ZnAc_2 \cdot 2H_2O$ and $CoAc_2 \cdot 4H_2O$ were adjusted according to the desired solid solution composition, x , where x is the nominal Co fraction in the precursor solutions as calculated from the ratio of the moles of $CoAc_2$ to the sum of the moles of $CoAc_2$ and $ZnAc_2$ (*i.e.*, $[CoAc_2]/[Co(II)Ac_2 + ZnAc_2]$). Following this, 4.0×10^{-3} mol of thiourea and 3.4×10^{-3} mol of $HSCH_2COONa$ were added to the metal acetate solution. After sonication for 30 minutes, this mixture was sealed in a Teflon vial, placed inside a SiC sleeve, and loaded into an Anton Parr Multiwave Pro microwave. The solution temperature was measured using an infrared sensor. The solution was heated from room temperature to 160 °C in 15 minutes and maintained at 160 °C for 5 minutes. Following this, the power was turned off, and the solution was cooled to 55 °C in approximately 20 minutes with the aid of the fans inside the microwave. The microwave is equipped with a turntable, which spins at 2 revolutions per minute (RPM) during the entire synthesis, but the solution is not stirred. Using conventional heating, instead of microwave heating, produces a brown amorphous powder as evidenced by the lack of any XRD peaks.

Formation of polycrystalline films

After synthesis, the wurtzite $Cu_2(Zn_{1-x}Co_x)SnS_4$ nanocrystals were centrifuged at 8450 RCF for 15 minutes, the ethylene glycol supernatant was discarded, and the remaining nanocrystals were dispersed in water to make 36 ± 10 mg mL⁻¹ dispersions. These dispersions agglomerate in approximately one day and must be redispersed by sonication before use. The nanocrystal coatings were cast from dispersions that were sonicated for at least 1 hour prior to casting. Soda lime glass substrates covered with 700 nm of Mo were coated with the wurtzite $Cu_2(Zn_{1-x}Co_x)SnS_4$ nanocrystals by drop casting 400 μ L of the aqueous dispersions onto 6.25 cm² area defined by a metal frame. After drop casting, the coatings were dried at room temperature for 2 days as described previously.^{35,36} The substrates coated with nanocrystals were annealed in air at 200 °C for 10 minutes to remove any residual

water trapped in between the nanocrystals. These nanocrystal coatings were porous and rough because the nanocrystals agglomerate as the dispersion cast on the substrate dries. The coatings were compacted using a hydraulic press at 6000 kPa for 15 seconds (Caver Autopellet 3887) as described previously.^{37,38} A thin sheet of Kapton film was placed on top of the nanocrystal coating to prevent the nanocrystals from adhering to the press.

The compacted wurtzite $\text{Cu}_2(\text{Zn}_{1-x}\text{Co}_x)\text{SnS}_4$ nanocrystal coatings were placed in pre-cleaned quartz ampoules (1 cm inner diameter and 10 cm length) with 14 mg of solid sulfur and 3×10^{-5} moles of NaOH, which were introduced as described by Johnson *et al.*³⁹ Following this, the quartz ampoule was evacuated to 10^{-6} Torr and flame-sealed. The sealed quartz ampoule at room temperature was loaded into a preheated furnace at 600 °C. At this temperature, 14 mg of sulfur corresponds to approximately 500 Torr of sulfur vapor. Details of the annealing process can be found in our previous papers.^{19,37,39} After maintaining the quartz ampoule at 600 °C for 1 hour, the furnace was turned off and the ampoule was allowed to cool naturally to 150 °C before removing it from the furnace. The furnace took approximately 4 hours to cool to 150 °C.

Characterization

The nanocrystal coatings were characterized, before and after annealing in sulfur, using X-ray diffraction (XRD), Raman scattering, optical absorption, and field emission scanning electron microscopy (FE-SEM). The as-synthesized nanocrystals were also characterized using transmission electron microscopy (TEM). Specifically, XRD patterns from the products were collected using a PANalytical X'Pert Pro X-ray diffractometer (Co $K\alpha$ radiation with a wavelength of 1.7890 Å) equipped with an X'Celerator detector. The XRD patterns were collected from 20 to 70° (2θ) with an effective step size of 0.0167° and 50 s dwell time per step. Lattice parameters were calculated by Rietveld refinement using the X'pert High Score Plus software. Raman spectra were collected from dried powders and annealed thin films using a Witec Confocal micro-Raman spectrometer, with a green (532 nm) laser as the excitation source. The laser power was fixed at 1 mW, and each spectrum was integrated over 150 seconds. The absorption spectra were collected in the transmission mode using an Agilent Cary 5000 UV-Vis-NIR spectrometer. A constant small background below the bandgap due to reflection and scattering was subtracted from each spectrum. For FE-SEM examination, the nanocrystals dispersed in methanol were sonicated for 1 hour, dropcast onto soda lime glass substrates, and dried in air. The dried nanocrystal coatings and annealed thin films were then examined on a JEOL 6500 FE-SEM, at an acceleration voltage of 5 kV. The elemental composition of the nanocrystals was determined using energy dispersive X-ray spectroscopy (EDS) using a Thermo-Noran Vantage system equipped with an EDS detector coupled to the JEOL 6500 FE-SEM. The acceleration voltage was adjusted to 15 kV for all EDS measurements. The ratios of the elemental concentrations were calculated based on the reference spectra provided by the software system SIX and converted to atomic%. For each sample, the elemental compositions were determined

at ten different locations and the values were averaged. Grain sizes were estimated from SEM images of the thin films by randomly drawing lines on several plan view SEM images and the average grain sizes were determined from the number of grain boundaries intersected by the line per unit length. Samples for TEM characterization were prepared by drop casting nanocrystals onto Ni TEM grids (SPI 200 mesh holey carbon coated) from methanol dispersions after sonication for at least 30 minutes. The nanocrystals were imaged using an FEI T12 TEM, operating at an accelerating voltage of 120 kV. High-resolution images were collected using an FEI Tecnai G2 F30, with an accelerating voltage of 300 kV. The elemental composition of the nanocrystals was also measured using inductively coupled plasma mass spectroscopy (ICP-MS) using a Thermo Scientific XSERIES 2 ICP-MS with an ESI PC3 Peltier cooled spray chamber, SC-FAST injection loop, and SC-4 auto sampler. Samples were diluted as appropriate and 40 ppb of indium internal standard was added. The powders were digested in a mixture of 4 mL of concentrated trace metal grade HNO_3 , 1 mL of deionized water, 1.5 mL of concentrated trace metal grade HCl, and 1.5 mL of concentrated trace metal grade HF. The powders were digested by heating this dispersion in a CEM Corp Discover SP-D microwave to 150 °C for 4 minutes. We use a capital X to denote the measured (by ICP-MS and SEM-EDS) Co fraction, which is defined as $C_{\text{Co}}/(C_{\text{Zn}} + C_{\text{Co}})$ in the nanocrystals, where C_i is the concentration of species i (Co or Zn). We use small x in $\text{Cu}_2(\text{Zn}_{1-x}\text{Co}_x)\text{SnS}_4$ nanocrystals to denote the nominal Co fraction calculated from the ratio of the moles of Co(II) acetate monohydrate to the sum of Co(II) acetate monohydrate and Zn(II) acetate monohydrate in the precursor solutions. These values (X and x) are within measurement error and are virtually the same as shown in ESI Fig. S1.† Even though Na is present in the synthesis, it was not detected in the product. If present, its concentration is below the detection limit of EDS ($\sim 0.3\%$).

Results and discussion

$\text{Cu}_2(\text{Zn}_{1-x}\text{Co}_x)\text{SnS}_4$ nanocrystals

Fig. 1 shows (a) XRD patterns, (b) lattice parameters, and (c) sizes of $\text{Cu}_2(\text{Zn}_{1-x}\text{Co}_x)\text{SnS}_4$ nanocrystals as a function of x . All XRD patterns show three strong peaks located near 30.5°, 32°, and 35°, which correspond to diffraction from the (100), (002), and (101) planes in wurtzite $\text{Cu}_2(\text{Zn}_{1-x}\text{Co}_x)\text{SnS}_4$ ($P6_3mc$). Additionally, the XRD patterns exhibit several weak diffraction peaks near 46°, 55°, 60°, and 66°, corresponding to the (102), (110), (103), and (112) planes, also in wurtzite $\text{Cu}_2(\text{Zn}_{1-x}\text{Co}_x)\text{SnS}_4$.⁴⁰ No secondary phases such as Zn-, Sn-, Cu- and Co-based sulfide compounds are detected regardless of x . Generally, the relative intensities of the XRD peaks are consistent with those expected for a powder diffraction pattern of the wurtzite phase, indicating that the kesterite and/or stannite phases are present at very low concentrations or completely absent; were a significant fraction of these phases present, the (002) peak intensity would have increased substantially as compared to the (100) and (101) peaks (see ESI Fig. S2†). In fact, careful examination of the XRD patterns for samples with $x = 0$ and $x = 0.05$ shows that the

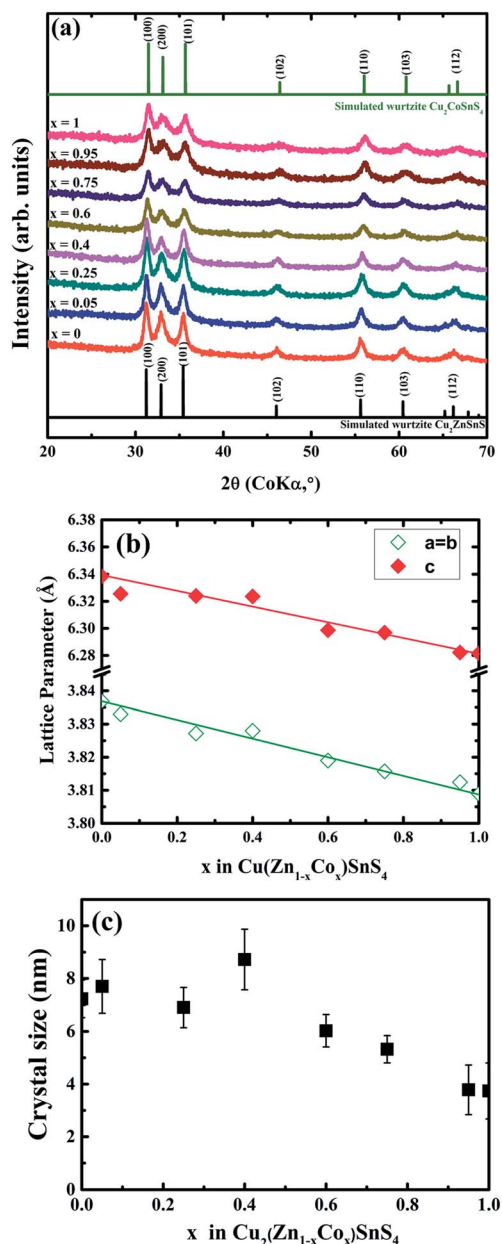


Fig. 1 (a) XRD patterns, (b) lattice parameters, and (c) sizes of $\text{Cu}_2(\text{Zn}_{1-x}\text{Co}_x)\text{SnS}_4$ nanocrystals as a function of the Co fraction, x . Simulated XRD patterns of wurtzite $\text{Cu}_2\text{ZnSnS}_4$ and $\text{Cu}_2\text{CoSnS}_4$ are shown as stick patterns. Lines in (b) are linear extrapolation (Vegard's law) between the lattice parameters of $\text{Cu}_2\text{ZnSnS}_4$ and $\text{Cu}_2\text{CoSnS}_4$. Nanocrystal sizes were obtained from the Scherrer equation using the measured XRD patterns. Co $K\alpha$ emission was used for XRD. Also see ESI Fig. S2† for XRD patterns on an expanded scale between $2\theta = 30^\circ$ and $2\theta = 37^\circ$, and for simulation details.

(002) peak is slightly higher than expected for wurtzite, indicating the possible presence of small amounts of the kesterite phase. The a and c lattice parameters in the wurtzite $\text{Cu}_2(\text{Zn}_{1-x}\text{Co}_x)\text{SnS}_4$ nanocrystals decrease with increasing Co fraction, x , because the ionic radius of Co^{2+} (0.68 Å) is smaller than the ionic radius of Zn^{2+} (0.88 Å). For $x = 0$ and $x = 1$ wurtzite $\text{Cu}_2\text{ZnSnS}_4$ and wurtzite $\text{Cu}_2\text{CoSnS}_4$, the calculated

lattice parameters are in excellent agreement with those reported previously (Table 1).^{4,41,42}

The sizes of the $\text{Cu}_2(\text{Zn}_{1-x}\text{Co}_x)\text{SnS}_4$ nanocrystals, calculated from the full width at half maximum of the (002) diffraction peak using the Scherrer equation, remain approximately constant up to $x = 0.5$ and decrease thereafter. The decrease in the nanocrystal size with increasing doping or alloying (*i.e.* increasing x) has been observed previously in other systems⁴³ and may be expected when two different types of ions compete for the same lattice position because this competition can reduce both the nucleation and the growth of the nanocrystals.^{44,45} For example, lattice strain induced upon incorporation of ions with different radii can increase the critical nucleation size.

Fig. 2 shows the Raman spectra of the $\text{Cu}_2(\text{Zn}_{1-x}\text{Co}_x)\text{SnS}_4$ nanocrystals as a function of nominal Co fraction, x . The A_1 mode peak position shifts from 328 cm^{-1} for $x = 0$ ($\text{Cu}_2\text{ZnSnS}_4$) to 319 cm^{-1} for $x = 1$ ($\text{Cu}_2\text{CoSnS}_4$). The A_1 mode peak in wurtzite CZTS has been reported to range from 325 cm^{-1} to 335 cm^{-1} .^{50–54} There is evidence that the A_1 mode peak position may depend on the shape and size of the nanocrystals.^{19–23} For example, Li *et al.* reported the A_1 mode peak position for wurtzite CZTS nanoplates at 335 cm^{-1} as compared to 325 cm^{-1} for oblate rice shaped nanocrystals.⁵¹ Our nanocrystals were a mixture of oblate and spherical nanocrystals (*vide infra*) and gave rise to a broad Raman scattering peak that peaked at 328 cm^{-1} for wurtzite CZTS ($x = 0$). To our knowledge, there is no Raman scattering reported for wurtzite $\text{Cu}_2\text{CoSnS}_4$. Gillorin *et al.* synthesized kesterite $\text{Cu}_2\text{Co}_x\text{SnS}_4$ and reported a broad Raman scattering peak peaking at 315 cm^{-1} for 3 nm diameter nanocrystals.²⁵ For larger $\text{Cu}_2\text{CoSnS}_4$ kesterite crystals (*e.g.*, 100 s of nm), Krishnaiah observed the A_1 peak at 325 cm^{-1} .²⁹ Huang *et al.* reported a shift from 335 cm^{-1} to 325 cm^{-1} for stannite or kesterite $\text{Cu}_2(\text{Zn}_{1-x}\text{Co}_x)\text{SnS}_4$ as x increased from 0 to 1.³¹ Thus, substituting Co for Zn in kesterite CZTS appears to shift the A_1 mode from 337 cm^{-1} to 325 cm^{-1} . Such a Raman shift to lower wavenumbers has also been observed when Zn was substituted with Fe to form $\text{Cu}_2(\text{Zn}_{1-x}\text{Fe}_x)\text{SnS}_4$ and Co to form $\text{Cu}_2(\text{Zn}_{1-x}\text{Co}_x)\text{SnS}_4$.⁵⁵ Both alloying and the small nanocrystal size broaden the Raman peaks and reduce the scattering intensity, making it difficult to ascertain the phase purity by Raman measurements alone. However, there is no obvious presence of large amounts of secondary phases such as Cu-, Zn-, Co-, and Sn-sulfides *via* XRD. The impurity phases that are most difficult to distinguish from $\text{Cu}_2(\text{Zn}_{1-x}\text{Co}_x)\text{SnS}_4$ are Cu_3SnS_4 and ZnS. ZnS Raman scattering at $\sim 350\text{ cm}^{-1}$ is weak and can be easily masked by the main broad A_1 mode.^{56–58} Similarly, the most intense Raman scattering from Cu_3SnS_4 is at 318 cm^{-1} .⁵⁶ To complicate matters, these phases have overlapping XRD peaks with $\text{Cu}_2(\text{Zn}_{1-x}\text{Co}_x)\text{SnS}_4$. However, the presence of both of these phases in significant amounts would alter the intensity ratios of the (100), (002), and (101) XRD peaks as shown in Fig. 1. This is not the case and the diffraction intensity ratios closely match those expected from a powder of $\text{Cu}_2(\text{Zn}_{1-x}\text{Co}_x)\text{SnS}_4$.

Fig. 3 shows the representative high resolution (HR)-TEM images of $\text{Cu}_2(\text{Zn}_{1-x}\text{Co}_x)\text{SnS}_4$ nanocrystals. The

Table 1 Lattice parameters of the $\text{Cu}_2(\text{Zn}_{1-x}\text{Co}_x)\text{SnS}_4$ phases

	Crystal structure	Space group	a (Å)	c (Å)
$\text{Cu}_2\text{ZnSnS}_4$ ($x = 0$) ref. 46	Wurtzite	$P6_3mc$	3.8387	6.3388
$\text{Cu}_2\text{CoSnS}_4$ ($x = 1$) ref. 47	Wurtzite	$P6_3mc$	3.806	6.295
$\text{Cu}_2\text{ZnSnS}_4$ ($x = 0$) ref. 48	Kesterite	$I4_{2m}$	5.427	10.848
$\text{Cu}_2\text{CoSnS}_4$ ($x = 1$) ref. 49	Kesterite	$I4_{2m}$	5.396	10.789
$\text{Cu}_2\text{ZnSnS}_4$ ($x = 0$) this work	Wurtzite	$P6_3mc$	3.837	6.339
$\text{Cu}_2\text{CoSnS}_4$ ($x = 1$) this work	Wurtzite	$P6_3mc$	3.809	6.281

$\text{Cu}_2(\text{Zn}_{1-x}\text{Co}_x)\text{SnS}_4$ nanocrystals are either spherical or oblate. Oblate nanocrystals have been observed previously when wurtzite $\text{Cu}_2\text{ZnSnS}_4$ and $\text{Cu}_2\text{CoSnS}_4$ nanocrystals were synthesized in other solvents.^{26,41} On average the nanocrystals observed in the TEM are smaller for larger x , which is consistent with sizes obtained from the XRD patterns (Fig. 1(c)). The HRTEM images show lattice fringes with spacings consistent with the (101), (102), (100) planes of wurtzite CZTS and wurtzite $\text{Cu}_2\text{CoSnS}_4$. The fast Fourier transform (FFT) patterns well match with the wurtzite structure of $\text{Cu}_2(\text{Zn}_{1-x}\text{Co}_x)\text{SnS}_4$ and are shown in the ESI (Fig. S3†).

The $\text{Cu}_2(\text{Zn}_{1-x}\text{Co}_x)\text{SnS}_4$ nanocrystals show strong absorption in the visible region of the electromagnetic spectrum, with the absorption edge (Fig. 4) blue shifting from ~ 1120 nm (1.1 eV) to ~ 920 nm (1.35 eV) as x is increased. The band gap of wurtzite

$\text{Cu}_2\text{ZnSnS}_4$ has been reported to be between 1.4 and 1.5 eV, but these analyses rely on plotting $(\alpha h\nu)^2$ vs. $(h\nu)$, arbitrarily deciding the region where this plot appears linear, and extrapolating this line to $(\alpha h\nu) = 0$ to find where it intercepts the $(h\nu)$ axis; this intercept is an estimate of the band gap energy, E_g .⁵⁹ However, this analysis is fraught with difficulties and potential pitfalls, particularly when there is significant reflection and scattering or when there is absorption near the band edge due to plasmons or tail states. Indeed, all the reported measurements for wurtzite CZTS show absorption below the reported band gap values^{41,46,59} (see also the discussion in the ESI†). Using density functional theory within hybrid functional PBE0, Zhao *et al.* calculated the wurtzite CZTS band gap to be 1.372 eV.⁶⁰ Like the previous experimental absorption spectra, absorption from our wurtzite CZTS films also begins to rise at ~ 1200 nm, indicating either a lower band gap value than the reported 1.43 eV or a significant absorption tail below the conduction band edge, possibly due to defects. There is only one report of optical absorption in $\text{Cu}_2(\text{Zn}_{1-x}\text{Co}_x)\text{SnS}_4$, but these are in kesterite or stannite nanocrystals.³¹ Based on the changes in the Raman peak widths, the authors claimed that the crystal structure changed from kesterite to stannite, around $x = 0.3-0.6$, as x was increased. The XRD, however, shows that these crystals were either kesterite or stannite and not wurtzite. These authors reported that the band gap of $\text{Cu}_2(\text{Zn}_{1-x}\text{Co}_x)\text{SnS}_4$ (kesterite or stannite) red shifted from 1.45 eV at $x = 0$ to 1.21 eV at $x = 1$. These values are again determined from extrapolation of the $(\alpha h\nu)^2$ vs. $(h\nu)$ plot, which showed a significant tail and absorption below the extrapolated values. In fact, one cannot discern a band edge from the unprocessed absorption spectra in this article. Our absorption edge gradually blue shifts to ~ 1.35 eV as more Co is substituted for Zn (*i.e.*, x increases), the opposite trend to that reported by Huang *et al.*³¹ (see also the discussion in the ESI†). One possibility is that the nanocrystals become increasingly more quantum confined as their sizes decrease with increasing Co concentration (see Fig. 1), but Khare *et al.* showed that the CZTS nanocrystal sizes must be approximately 3 nm or less to observe this effect.⁶¹ Thus, quantum confinement is an unlikely explanation for the shift observed in the spectra of Fig. 4.

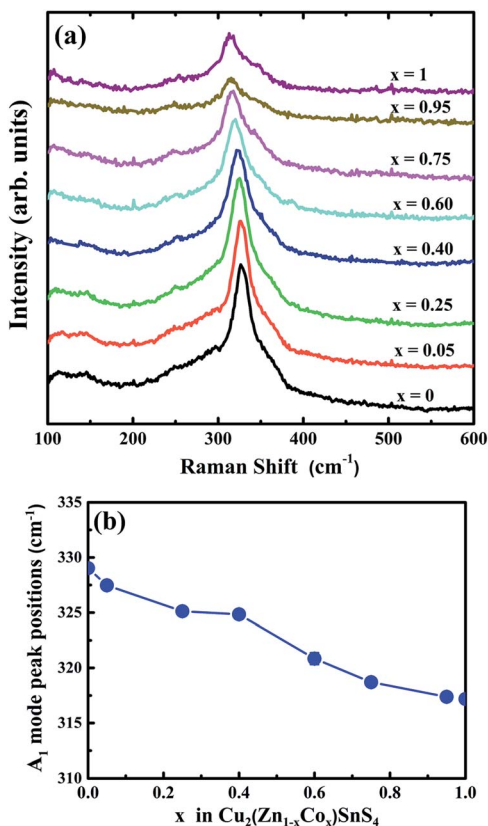


Fig. 2 (a) Raman spectra and (b) A_1 mode peak positions of $\text{Cu}_2(\text{Zn}_{1-x}\text{Co}_x)\text{SnS}_4$ nanocrystals as a function of x .

Polycrystalline $\text{Cu}_2(\text{Zn}_{1-x}\text{Co}_x)\text{SnS}_4$ thin films

Encouraged by the formation of wurtzite $\text{Cu}_2(\text{Zn}_{1-x}\text{Co}_x)\text{SnS}_4$ solid solutions without any detectable secondary phases, we proceeded to study the formation of polycrystalline $\text{Cu}_2(\text{Zn}_{1-x}\text{Co}_x)\text{SnS}_4$ thin films from coatings comprising the nanocrystals. We made

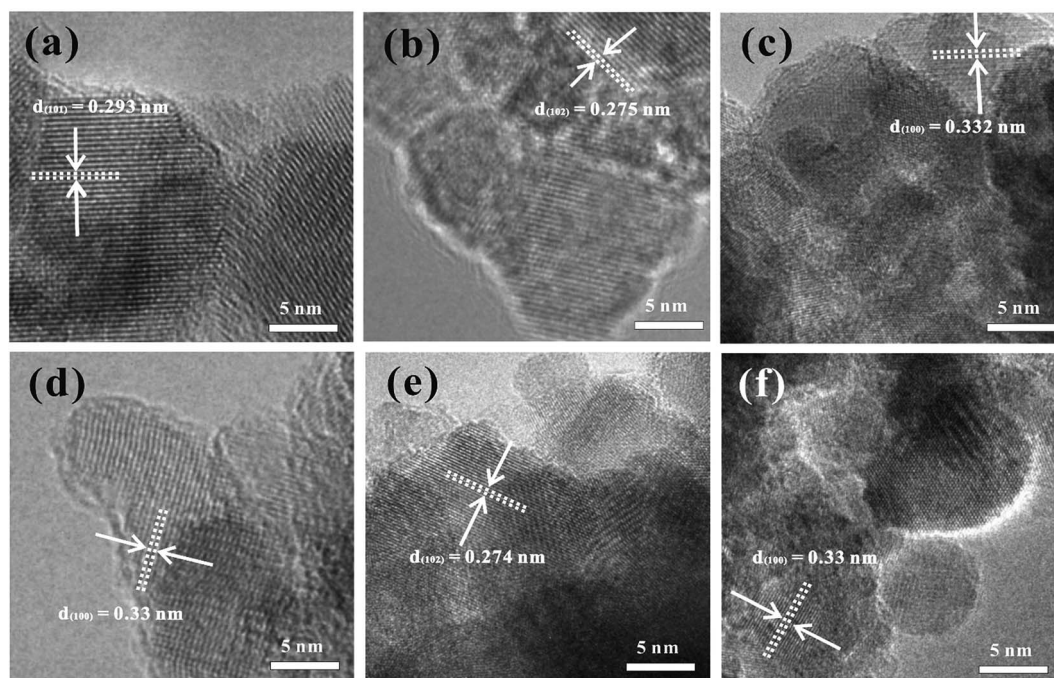


Fig. 3 Representative TEM images of $\text{Cu}_2(\text{Zn}_{1-x}\text{Co}_x)\text{SnS}_4$ nanocrystals with (a) $x = 0$, (b) $x = 0.25$, (c) $x = 0.4$, (d) $x = 0.6$, (e) $x = 0.75$, and (f) $x = 1$, respectively. TEM samples were made by drop casting the nanocrystal dispersion in methanol onto Ni carbon mesh grids.

polycrystalline $\text{Cu}_2(\text{Zn}_{1-x}\text{Co}_x)\text{SnS}_4$ thin films by annealing, in sulfur vapor, coatings dropcast onto Mo-coated soda lime glass substrates from aqueous dispersions of the nanocrystals. Fig. 5 shows the XRD patterns and lattice parameters of the polycrystalline films formed on Mo-coated soda lime glass substrates by annealing coatings of $\text{Cu}_2(\text{Zn}_{1-x}\text{Co}_x)\text{SnS}_4$ nanocrystals. The XRD patterns collected from the annealed films with $x = 0$ are

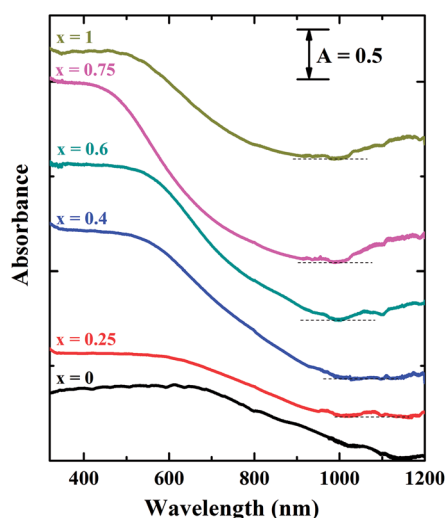


Fig. 4 Optical absorption spectra of $\text{Cu}_2(\text{Zn}_{1-x}\text{Co}_x)\text{SnS}_4$ nanocrystals as a function of Co fraction, x . The absorption spectra were obtained from films dropcast from nanocrystal dispersions in methanol on soda lime glass substrates after compaction. The baseline was offset for $x > 0$ for clarity. The baseline for the offset spectra ($A = 0$) is indicated with a dashed line.

consistent with the kesterite CZTS phase, Mo, and MoS_2 . When annealed, the wurtzite nanocrystals transform into larger kesterite grains. When x is less than 0.4, no secondary phases were detected by XRD, and the films appear to consist primarily of polycrystalline $\text{Cu}_2(\text{Zn}_{1-x}\text{Co}_x)\text{SnS}_4$. On the other hand, when $x \geq 0.6$, secondary phases such as $\text{Cu}_{1.96}\text{S}$ and $\text{Co}_{0.24}\text{Zn}_{0.76}\text{S}$ were also detected. We assign the peak appearing at 33.4° to cubic $\text{Co}_{0.24}\text{Zn}_{0.76}\text{S}$. This peak appears at around $x = 0.75$ and increases in intensity as the Co concentration is increased and x reaches 1. It may seem odd that this particular composition of this alloy forms, but Becker and Lutz *et al.* showed that there is a limit to the solubility of Co in zinc blende ZnS . It so happens that 24% is indeed the solubility limit at 600°C , our annealing temperature.⁶² The diffraction peaks at 22° and 45.6° are from tetragonal $\text{Cu}_{1.96}\text{S}$. The Mo peak at 38° overlaps with diffraction from some of the secondary phases, most notably the strong (103) diffraction from $\text{Cu}_{1.96}\text{S}$ also at 38° . One can still see the $\text{Cu}_{1.96}\text{S}$ diffraction emerging from the top of the broad Mo diffraction for films with $x = 0.6$ and $x = 0.75$. Although wurtzite $\text{Cu}_2(\text{Zn}_{1-x}\text{Co}_x)\text{SnS}_4$ forms across the entire composition range, kesterite $\text{Cu}_2(\text{Zn}_{1-x}\text{Co}_x)\text{SnS}_4$ *via* this route could only be formed up to $x = 0.4$. It is interesting to note that $\text{Cu}_2(\text{Zn}_{1-x}\text{Fe}_x)\text{SnS}_4$ transforms from kesterite to stannite with changes in the cation ordering when $x \approx 0.4-0.5$.^{49,63,64} Because Co^{2+} and Fe^{2+} have similar sizes, like $\text{Cu}_2(\text{Zn}_{1-x}\text{Fe}_x)\text{SnS}_4$, kesterite $\text{Cu}_2(\text{Zn}_{1-x}\text{Co}_x)\text{SnS}_4$ also becomes destabilized near this value of x .³¹ For this reason, we surmise that the formation of kesterite from the wurtzite structure may become inaccessible around $x \approx 0.4-0.5$, leading instead to phase separation into $\text{Cu}_{1.96}\text{S}$ and $\text{Co}_{0.24}\text{Zn}_{0.76}\text{S}$.

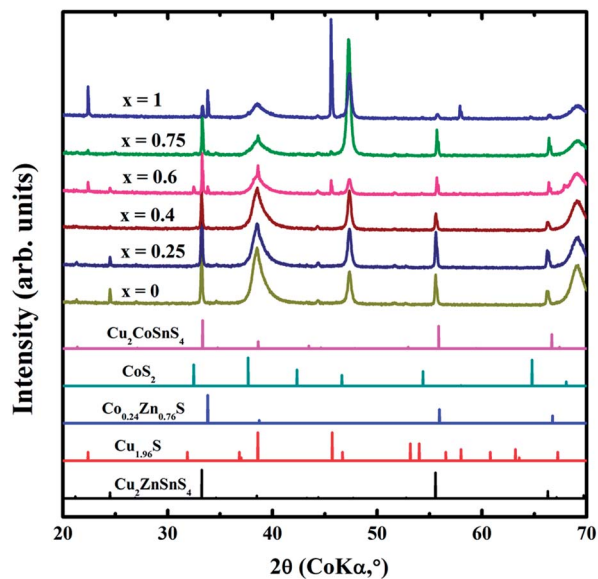


Fig. 5 XRD patterns of $\text{Cu}_2(\text{Zn}_{1-x}\text{Co}_x)\text{SnS}_4$ polycrystalline thin films formed on Mo-coated soda lime glass substrates via thermal annealing, in sulfur, of $\text{Cu}_2(\text{Zn}_{1-x}\text{Co}_x)\text{SnS}_4$ nanocrystal coatings. Annealing was conducted in 500 Torr of sulfur at 600 °C for 1 hour. 3.0×10^{-5} mol of Na was added to the annealing ampule as described in the experimental procedure. The XRD patterns of kesterite $\text{Cu}_2\text{ZnSnS}_4$ (00-026-0575), kesterite $\text{Cu}_2\text{CoSnS}_4$ (00-026-0513), tetragonal $\text{Cu}_{1.96}\text{S}$ (00-012-0224), cubic $\text{Co}_{0.24}\text{Zn}_{0.76}\text{S}$ (00-047-1656), and cubic CoS_2 (98-001-3473) are also shown for comparison. Co K α emission was used for XRD.

The lattice parameters of polycrystalline $\text{Cu}_2(\text{Zn}_{1-x}\text{Co}_x)\text{SnS}_4$ thin films extracted from the XRD decrease from $a = 0.5429$ nm and $c = 1.0832$ nm at $x = 0$ to $a = 0.5425$ nm and $c = 1.0828$ nm at $x = 0.4$, and this trend is consistent with the results obtained with the $\text{Cu}_2(\text{Zn}_{1-x}\text{Co}_x)\text{SnS}_4$ nanocrystals (Fig. 1(b)). For $x \geq 0.4$, we cannot determine the true x in the kesterite phase since there are significant secondary phases in the films. Annealing at 500 °C showed similar results to annealing at 600 °C in that the films with $x \leq 0.4$ were phase pure kesterite, but, for $x \geq 0.6$, secondary phases such as $\text{Cu}_{1.96}\text{S}$ and $\text{Co}_{0.24}\text{Zn}_{0.76}\text{S}$ were also detected. On the other hand, the grain sizes of films annealed at 500 °C were smaller (0.1–0.6 μm) than those at 600 °C (0.5–2 μm).

Fig. 6 shows the Raman spectra and A_1 mode peak positions for polycrystalline $\text{Cu}_2(\text{Zn}_{1-x}\text{Co}_x)\text{SnS}_4$ thin films formed on Mo-coated soda lime glass substrates. The film made from nanocrystals without Co ($x = 0$) exhibits a strong peak located at 337 ± 2 cm^{-1} , which corresponds to the A_1 mode Raman peak of the kesterite CZTS structure. As x increases to $x = 0.4$ (Fig. 6(a)), this peak shifts towards lower wavenumbers (324 cm^{-1}), broadens, and decreases in intensity. This behavior would be expected if Co was substituting for Zn and forming a solid solution. If the Co and Zn were to phase segregate into $\text{Cu}_2\text{ZnSnS}_4$ and $\text{Cu}_2\text{CoSnS}_4$ domains, we would expect two sharper peaks, with one at 337 cm^{-1} for $\text{Cu}_2\text{ZnSnS}_4$ and the other around 324 cm^{-1} for $\text{Cu}_2\text{CoSnS}_4$.^{29,31} For $x \leq 0.4$, we do not observe any other Raman scattering that can be assigned to secondary phases. However, we begin seeing Raman scattering from secondary phases in films synthesized with $x \geq 0.6$, in addition to that

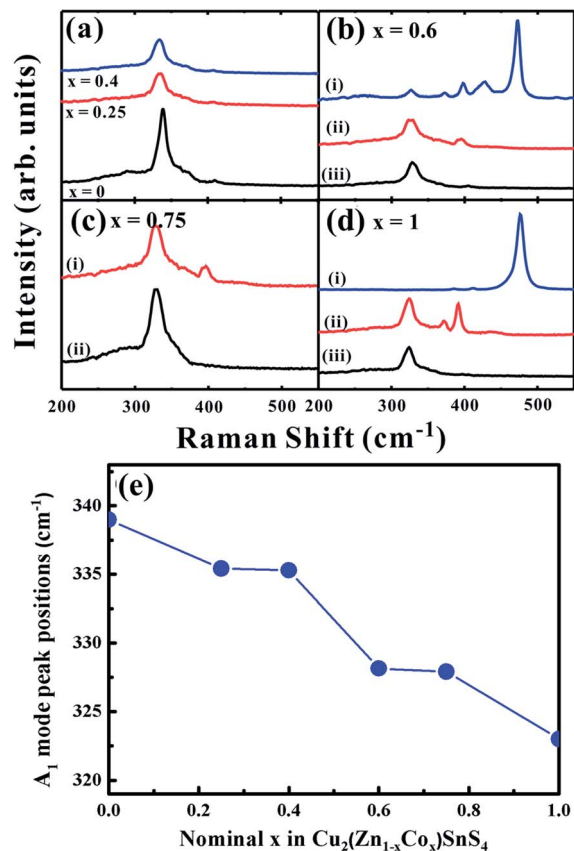


Fig. 6 (a–d) Raman spectra and (e) A_1 mode peak positions of $\text{Cu}_2(\text{Zn}_{1-x}\text{Co}_x)\text{SnS}_4$ thin films formed on Mo coated soda lime glass substrates by thermal annealing of $\text{Cu}_2(\text{Zn}_{1-x}\text{Co}_x)\text{SnS}_4$ nanocrystal coatings. A_1 mode Raman peaks were collected from large grains in the $\text{Cu}_2(\text{Zn}_{1-x}\text{Co}_x)\text{SnS}_4$ films as shown in (e). Annealing conditions were the same as for Fig. 5. The Raman spectra of $\text{Cu}_2(\text{Zn}_{1-x}\text{Co}_x)\text{SnS}_4$ thin films at $x \geq 0.6$ (b–d) were collected from different grains, which were selected to show the different phases present.

from kesterite $\text{Cu}_2(\text{Zn}_{1-x}\text{Co}_x)\text{SnS}_4$, which appears between 337 cm^{-1} ($x = 0$) and 324 cm^{-1} ($x = 1$). For example, Fig. 6(b) shows Raman spectra collected from three different locations on the same film ($x = 0.6$). Region (i) shows intense Raman scattering from copper–sulfur vibrations characteristic of copper sulfides (475 cm^{-1}). An additional peak at 400 cm^{-1} can be identified both in this region (i) and elsewhere on the film, e.g., region (ii), and is assigned to characteristic Co–S vibrations in $\text{Co}_{0.24}\text{Zn}_{0.76}\text{S}$, which are expected around 390 – 400 cm^{-1} .^{65,66} Region (ii) in Fig. 6(b) shows Raman scattering from $\text{Cu}_2(\text{Zn}_{1-x}\text{Co}_x)\text{SnS}_4$ and $\text{Co}_{0.24}\text{Zn}_{0.76}\text{S}$ but not from $\text{Cu}_{1.96}\text{S}$. The vast majority of the film, however, is $\text{Cu}_2(\text{Zn}_{1-x}\text{Co}_x)\text{SnS}_4$ and exhibits Raman scattering like that shown for region (iii) in Fig. 6(b). In some regions like region (i) in Fig. 6(d) a particularly strong Raman peak at 476 cm^{-1} from copper sulfide is observed when $x = 1$.

Fig. 7 shows the plan view and cross-sectional FE-SEM images of the polycrystalline thin films formed on Mo-coated soda lime glass substrates via thermal annealing of $\text{Cu}_2(\text{Zn}_{1-x}\text{Co}_x)\text{SnS}_4$ nanocrystal coatings in sulfur. FE-SEM images of the polycrystalline $\text{Cu}_2(\text{Zn}_{1-x}\text{Co}_x)\text{SnS}_4$ thin film for

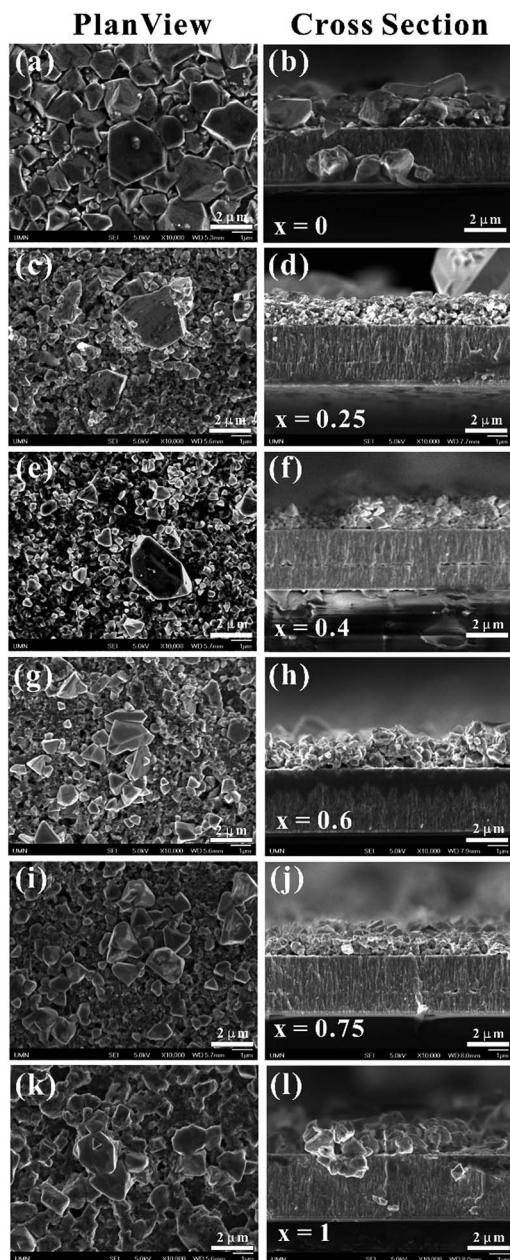


Fig. 7 Plan view and cross-sectional FE-SEM images of the $\text{Cu}_2(\text{Zn}_{1-x}\text{Co}_x)\text{SnS}_4$ thin films formed on Mo coated soda lime glass substrates by thermal annealing of the $\text{Cu}_2(\text{Zn}_{1-x}\text{Co}_x)\text{SnS}_4$ nanocrystal coating: ((a) and (b)) $x = 0$, ((c) and (d)) $x = 0.25$, ((e) and (f)) $x = 0.4$, ((g) and (h)) $x = 0.6$, ((i) and (j)) $x = 0.75$, and ((k) and (l)) $x = 1$. Annealing conditions were the same as for Fig. 5.

$x = 0$ show a $2.0 \mu\text{m}$ thick film consisting of submicron sized grains ranging from 0.2 to $2.4 \mu\text{m}$. The grains appear densely packed though some voids are visible. As the Co fraction, x , increases, the microstructure and grain size undergo dramatic changes. When $x = 0.25$ and 0.4 , we observe large abnormal grains that have grown to over $2 \mu\text{m}$ on top of a layer comprised of smaller 200 to 800 nm grains. The average grain size, increases from 0.6 ± 0.3 to $1.1 \pm 0.5 \mu\text{m}$ as x increases from 0.6 to 1 . Although the annealed $\text{Cu}_2(\text{Zn}_{1-x}\text{Co}_x)\text{SnS}_4$ thin films show

micron sized grains, there are also many voids. Further optimization of the annealing parameters, such as S partial pressure, temperature, and annealing time as well as Na concentration, will be needed.

Conclusions

We report the synthesis of wurtzite $\text{Cu}_2(\text{Zn}_{1-x}\text{Co}_x)\text{SnS}_4$ nanocrystals across the entire composition range using a microwave assisted solvothermal method. The $\text{Cu}_2(\text{Zn}_{1-x}\text{Co}_x)\text{SnS}_4$ nanocrystals have an average size that decreases from 8 to 4 nm as x increases from 0 to 1 . The absorption band edge blue shifted from 1.1 eV for $\text{Cu}_2\text{ZnSnS}_4$ ($x = 0$) to 1.35 eV for $\text{Cu}_2\text{Co}_x\text{SnS}_4$ ($x = 1$). These values are lower than those predicted by density functional theory calculations and previous attempts at determining the optical band gap for $\text{Cu}_2\text{ZnSnS}_4$ ($x = 0$) and $\text{Cu}_2\text{Co}_x\text{SnS}_4$ ($x = 1$). Either the band gaps of wurtzite $\text{Cu}_2\text{ZnSnS}_4$ ($x = 0$) and $\text{Cu}_2\text{Co}_x\text{SnS}_4$ ($x = 1$) are lower, or these materials have significant band tails due to defects. The lattice parameters of $\text{Cu}_2(\text{Zn}_{1-x}\text{Co}_x)\text{SnS}_4$ nanocrystals also decrease with increasing x . Finally, we made polycrystalline $\text{Cu}_2(\text{Zn}_{1-x}\text{Co}_x)\text{SnS}_4$ thin films by annealing, in sulfur vapor, coatings comprised of $\text{Cu}_2(\text{Zn}_{1-x}\text{Co}_x)\text{SnS}_4$ nanocrystals. Upon annealing, the coatings transformed into larger grained (100 s of nm to several microns) kesterite films if $x \leq 0.4$. At higher x ($x \geq 0.6$) annealing wurtzite nanocrystals produced secondary phases such as $\text{Co}_{0.24}\text{Zn}_{0.76}\text{S}$, $\text{Cu}_{1.96}\text{S}$ and Co_2S , in addition to kesterite $\text{Cu}_2(\text{Zn}_{1-x}\text{Co}_x)\text{SnS}_4$. Although this work shows that $\text{Cu}_2(\text{Zn}_{1-x}\text{Co}_x)\text{SnS}_4$ films can be synthesized for $x \leq 0.4$ from nanocrystal dispersions, it may be difficult to form phase pure films for higher values of x . Future work should focus on improving the film morphology and phase purity as well as on the electrical characterization of thin films towards making solar cells.

Conflicts of interest

There are no conflicts to declare.

Acknowledgements

This research was partially supported by the Environmental and Natural Resources Trust Fund (ENRTF) from the State of Minnesota and part of this work was carried out in the College of Science and Engineering Characterization Facility, University of Minnesota, which has received capital equipment funding from the NSF through the UMN MRSEC program under Award Number DMR-1420013.

Notes and references

- 1 H. Katagiri, N. Sasaguchi, S. Hando, S. Hoshino, J. Ohashi and T. Yokota, *Sol. Energy Mater. Sol. Cells*, 1997, **49**, 407–414.
- 2 D. B. Mitzi, O. Gunawan, T. K. Todorov, K. Wang and S. Guha, *Sol. Energy Mater. Sol. Cells*, 2011, **95**, 1421–1436.
- 3 K. Ito and T. Nakazawa, *Jpn. J. Appl. Phys.*, 1988, **27**, 2094–2097.

- 4 T. K. Todorov, K. B. Reuter and D. B. Mitzi, *Adv. Mater.*, 2010, **22**, E156–E159.
- 5 W. Shockley and H. J. Queisser, *J. Appl. Phys.*, 1961, **32**, 510–519.
- 6 J. Kim, H. Hiroi, T. K. Todorov, O. Gunawan, M. Kuwahara, T. Gokmen, D. Nair, M. Hopstaken, B. Shin, Y. S. Lee, W. Wang, H. Sugimoto and D. B. Mitzi, *Adv. Mater.*, 2014, **26**, 7427–7431.
- 7 P. Jackson, D. Hariskos, R. Wuerz, O. Kiowski, A. Bauer, T. M. Friedlmeier and M. Powalla, *Phys. Status Solidi RRL*, 2015, **9**, 28–31.
- 8 W. Ki and H. W. Hillhouse, *Adv. Energy Mater.*, 2011, **1**, 732–735.
- 9 G. Altamura and J. Vidal, *Chem. Mater.*, 2016, **28**, 3540–3563.
- 10 C. Yan, F. Liu, K. Sun, N. Song, J. A. Stride, F. Zhou, X. Hao and M. Green, *Sol. Energy Mater. Sol. Cells*, 2016, **144**, 700–706.
- 11 D. P. Halliday, R. Claridge, M. C. J. Goodman, B. G. Mendis, K. Durose and J. D. Major, *J. Appl. Phys.*, 2013, **113**, 223503–223512.
- 12 L. Van Puyvelde, J. Lauwaert, P. F. Smet, S. Khelifi, T. Ericson, J. J. Scragg, D. Poelman, R. Van Deun, C. Platzer-Björkman and H. Vrielinck, *Thin Solid Films*, 2015, **582**, 146–150.
- 13 T. Washio, H. Nozaki, T. Fukano, T. Motohiro, K. Jimbo and H. Katagiri, *J. Appl. Phys.*, 2011, **110**, 74511–74514.
- 14 A. D. Collord and H. W. Hillhouse, *Chem. Mater.*, 2016, **28**, 2067–2073.
- 15 Y. Cui, R. Deng, G. Wang and D. Pan, *J. Mater. Chem.*, 2012, **22**, 23136–23140.
- 16 M. J. Thompson, K. J. Blakeney, S. D. Cady, M. D. Reichert, J. Del Pilar-Albaladejo, S. T. White and J. Vela, *Chem. Mater.*, 2016, **28**, 1668–1677.
- 17 Q. Guo, H. W. Hillhouse and R. Agrawal, *J. Am. Chem. Soc.*, 2009, **131**, 11672–11673.
- 18 H. W. Hillhouse and M. C. Beard, *Curr. Opin. Colloid Interface Sci.*, 2009, **14**, 245–259.
- 19 B. D. Chernomordik, A. E. Béland, D. D. Deng, L. F. Francis and E. S. Aydil, *Chem. Mater.*, 2014, **26**, 3191–3201.
- 20 V. A. Akhavan, B. W. Goodfellow, M. G. Panthani, C. Steinhagen, T. B. Harvey, C. J. Stolle and B. A. Korgel, *J. Solid State Chem.*, 2012, **189**, 2–12.
- 21 C. Steinhagen, M. G. Panthani, V. Akhavan, B. Goodfellow, B. Koo and B. A. Korgel, *J. Am. Chem. Soc.*, 2009, **131**, 12554–12555.
- 22 H. Zhou, W.-C. Hsu, H.-S. Duan, B. Bob, W. Yang, T.-B. Song, C.-J. Hsu and Y. Yang, *Energy Environ. Sci.*, 2013, **6**, 2822–2838.
- 23 H. Yang, L. A. Jauregui, G. Zhang, Y. P. Chen and Y. Wu, *Nano Lett.*, 2012, **12**, 540–545.
- 24 A. D. Collord and H. W. Hillhouse, *Chem. Mater.*, 2015, **27**, 1855–1862.
- 25 A. Gillorin, A. Balocchi, X. Marie, P. Dufour and J. Y. Chane-Ching, *J. Mater. Chem.*, 2011, **21**, 5615–5619.
- 26 X. Zhang, N. Bao, B. Lin and A. Gupta, *Nanotechnology*, 2013, **24**, 105706–105713.
- 27 B. Murali and S. B. Krupanidhi, *J. Appl. Phys.*, 2013, **114**, 144312–144319.
- 28 B. Murali, M. Madhuri and S. B. Krupanidhi, *Cryst. Growth Des.*, 2014, **14**, 3685–3691.
- 29 M. Krishnaiah, P. Bhargava and S. Mallick, *RSC Adv.*, 2015, **5**, 96928–96933.
- 30 J. Zhong, Q. Wang and W. Cai, *Mater. Lett.*, 2015, **150**, 69–72.
- 31 K.-L. Huang, C.-H. Huang, W.-T. Lin, Y.-S. Fu and T.-F. Guo, *J. Alloys Compd.*, 2015, **646**, 1015–1022.
- 32 A. Hoshino, K. Fujioka, T. Oku, M. Suga, Y. F. Sasaki, T. Ohta, M. Yasuhara, K. Suzuki and K. Yamamoto, *Nano Lett.*, 2004, **4**, 2163–2169.
- 33 T. Andelman, S. Gordonov, G. Busto, P. V. Moghe and R. E. Riman, *Nanoscale Res. Lett.*, 2010, **5**, 263–273.
- 34 M. Baghbanzadeh, L. Carbone, P. D. Cozzoli and C. O. Kappe, *Angew. Chem., Int. Ed.*, 2011, **50**, 11312–11359.
- 35 B. D. Chernomordik, A. E. Béland, N. D. Trejo, A. A. Gunawan, D. D. Deng, K. a. Mkhoyan and E. S. Aydil, *J. Mater. Chem. A*, 2014, **2**, 10389–10395.
- 36 B. D. Chernomordik, P. M. Ketkar, A. K. Hunter, A. E. Béland, D. D. Deng and E. S. Aydil, *Chem. Mater.*, 2016, **28**, 1266–1276.
- 37 B. A. Williams, A. Mahajan, M. A. Smeaton, C. S. Holgate, E. S. Aydil and L. F. Francis, *ACS Appl. Mater. Interfaces*, 2015, **7**, 11526–11535.
- 38 B. A. Williams, M. A. Smeaton, C. S. Holgate, N. D. Trejo, L. F. Francis and E. S. Aydil, *J. Vac. Sci. Technol., A*, 2016, **34**, 51204–51213.
- 39 M. Johnson, S. V. Baryshev, E. Thimsen, M. Manno, X. Zhang, I. V. Veryovkin, C. Leighton and E. S. Aydil, *Energy Environ. Sci.*, 2014, **7**, 1931–1938.
- 40 A. H. Pinto, S. W. Shin, E. S. Aydil and R. L. Penn, *Green Chem.*, 2016, **18**, 5814–5821.
- 41 X. Lu, Z. Zhuang, Q. Peng and Y. Li, *Chem. Commun.*, 2011, **47**, 3141–3143.
- 42 A. Khare, B. Himmetoglu, M. Johnson, D. J. Norris, M. Cococcioni and E. S. Aydil, *J. Appl. Phys.*, 2012, **111**, 083707–083715.
- 43 S. Ghosh, M. Saha and S. K. De, *Nanoscale*, 2014, **6**, 7039.
- 44 J. D. Bryan, D. A. Schwartz and D. R. Gamelin, *J. Nanosci. Nanotechnol.*, 2005, **5**, 1472–1479.
- 45 R. Bose, G. Manna and N. Pradhan, *J. Phys. Chem. C*, 2013, **117**, 20991–20997.
- 46 W. Zhang, L. Zhai, N. He, C. Zou, X. Geng, L. Cheng, Y. Dong and S. Huang, *Nanoscale*, 2013, **5**, 8114–8121.
- 47 L. Shi, Y. Li, H. Zhu and Q. Li, *ChemPlusChem*, 2014, **79**, 1638–1642.
- 48 S. Das, R. M. Krishna, S. Ma and K. C. Mandal, *J. Cryst. Growth*, 2013, **381**, 148–152.
- 49 L. D. Gulay, O. P. Nazarchuk and I. D. Olekseyuk, *J. Alloys Compd.*, 2004, **377**, 306–311.
- 50 Y. Zhao, Q. Qiao, W.-H. Zhou, X.-Y. Cheng, D.-X. Kou, Z.-J. Zhou and S.-X. Wu, *Chem. Phys. Lett.*, 2014, **592**, 144–148.
- 51 M. Li, W.-H. Zhou, J. Guo, Y.-L. Zhou, Z.-L. Hou, J. Jiao, Z.-J. Zhou, Z.-L. Du and S.-X. Wu, *J. Phys. Chem. C*, 2012, **116**, 26507–26516.

- 52 A. Singh, H. Geaney, F. Laffir and K. M. Ryan, *J. Am. Chem. Soc.*, 2012, **134**, 2910–2913.
- 53 J. M. R. Tan, Y. H. Lee, S. Pedireddy, T. Baikie, X. Y. Ling and L. H. Wong, *J. Am. Chem. Soc.*, 2014, **136**, 6684–6692.
- 54 H. Guan, H. Hou, F. Yu and L. Li, *Mater. Lett.*, 2015, **159**, 200–203.
- 55 D. B. Khadka and J. Kim, *J. Phys. Chem. C*, 2014, **118**, 14227–14237.
- 56 A.-J. Cheng, M. Manno, A. Khare, C. Leighton, S. A. Campbell and E. S. Aydil, *J. Vac. Sci. Technol.*, 2011, **29**, 051203–051213.
- 57 M. Johnson, M. Manno, X. Zhang, C. Leighton and E. S. Aydil, *J. Vac. Sci. Technol.*, A, 2014, **32**, 61203–61212.
- 58 M. C. Johnson, C. Wrasman, X. Zhang, M. Manno, C. Leighton and E. S. Aydil, *Chem. Mater.*, 2015, **27**, 2507–2514.
- 59 C.-C. Kang, H.-F. Chen, T.-C. Yu and T.-C. Lin, *Mater. Lett.*, 2013, **96**, 24–26.
- 60 Z. Zhao, C. Ma, Y. Cao, J. Yi, X. He and J. Qiu, *Phys. Lett. A*, 2013, **377**, 417–422.
- 61 A. Khare, A. W. Wills, L. M. Ammerman, D. J. Norris and E. S. Aydil, *Chem. Commun.*, 2011, **47**, 11721–11723.
- 62 W. Becker and H. D. Lutz, *Mater. Res. Bull.*, 1978, **13**, 907–911.
- 63 P. Kevin, M. A. Malik, S. Mcadams and P. O'Brien, *J. Am. Chem. Soc.*, 2015, **137**, 15086–15089.
- 64 P. Bonazzi, L. Bindi, G. P. Bernardini and S. Menchetti, *Can. Mineral.*, 2003, **41**, 639–647.
- 65 C.-J. Chen, P.-T. Chen, M. Basu, K.-C. Yang, Y.-R. Lu, C.-L. Dong, C.-G. Ma, C.-C. Shen, S.-F. Hu and R.-S. Liu, *J. Mater. Chem. A*, 2015, **3**, 23466–23476.
- 66 S. G. Lyapin, A. N. Utyuzh, A. E. Petrova, A. P. Novikov, T. A. Lograsso and S. M. Stishov, *J. Phys.: Condens. Matter*, 2014, **26**, 396001–396007.